



# Sustainable water decontamination in a fluidic sequential electrochemical reactor

Mengjiao Xie<sup>a</sup>, Wentian Zheng<sup>a</sup>, Meng Sun<sup>b</sup>, Shijie You<sup>c</sup>, Yanbiao Liu<sup>a,d,\*</sup>

<sup>a</sup> College of Environmental Science and Engineering, Donghua University, Shanghai 201620 China

<sup>b</sup> Center for Water and Ecology, State Key Joint Laboratory of Environment Simulation and Pollution Control, School of Environment, Tsinghua University, Beijing 100084 China

<sup>c</sup> State Key Laboratory of Urban Water Resource and Environment, School of Environment, Harbin Institute of Technology, Harbin 150090 China

<sup>d</sup> School of Environmental Science and Technology, Key Laboratory of Industrial Ecology and Environmental Engineering (Ministry of Education), Dalian University of Technology, Dalian 116024, China.

## ARTICLE INFO

### Keywords:

O<sub>2</sub> self-feeding  
Sequential electrochemistry  
Nanoconfinement  
Singlet oxygen  
Water treatment

## ABSTRACT

Here, we demonstrate an integrated fluidic sequential electrochemical system for effective water decontamination. The system consists of a Ti mesh anode deposited with nanoscale IrO<sub>2</sub> and a CNT filter functionalized with nanoconfined Fe<sub>2</sub>O<sub>3</sub>. By conducting anodic oxygen evolution reaction (OER) and 2e<sup>-</sup> oxygen reduction reaction (ORR) sequential electrolysis, our system enables sustainable O<sub>2</sub> generation at the anode, followed by transformation of O<sub>2</sub> into H<sub>2</sub>O<sub>2</sub> at the cathode, which then led to the production of <sup>1</sup>O<sub>2</sub> in the presence of nanoconfined Fe<sub>2</sub>O<sub>3</sub>. No chemical inputs were needed nor side products occurred during the whole sequential electrochemical processes. The effectiveness of the system was evaluated using tetracycline as a model emerging contaminant. Recirculating at 3 mL min<sup>-1</sup>, the system exhibited negligible iron and iridium leaching (≤0.01 mg L<sup>-1</sup>) and high tetracycline degradation efficiency (≥95%). Such excellent efficacy can be maintained across a wide pH range and in complicated water matrices.

## 1. Introduction

As industry and urbanization have rapidly developed, interest has increased worldwide in the selective decontamination of a variety of emerging organic contaminants (EOCs) from water [1–3]. Existing biological processes are typically ineffective in dealing with these EOCs because of their high toxicity, low concentration and refractory structure [4–6]. Advanced oxidation processes (AOPs, e.g., the Fenton reaction and photocatalysis) have shown promising degradation capabilities by producing aggressive hydroxyl radicals (HO•) but susceptible to water constituents (e.g., natural organic matters) and environmental factors (e.g., solution pH). Thus, there is a huge need to establish new strategies to selectively and effectively degrade aqueous EOCs across a wide pH range.

One non-radical reactive oxygen species (ROS) that can selectively oxidize organic molecules is singlet oxygen (<sup>1</sup>O<sub>2</sub>) [7]. Compared with HO•, <sup>1</sup>O<sub>2</sub> has a relatively longer lifetime (μs vs ns), an extended migration distance, and encounters less interference from other constituents in water [8,9]. Numerous studies have confirmed that <sup>1</sup>O<sub>2</sub>

possesses a selective degradation ability for electron-rich organic compounds (e.g., sulfadiazine [10], sulfamethoxazole [9], and tetracycline (TC) [11]). To date, <sup>1</sup>O<sub>2</sub> is can be primarily synthesized through photosensitization [12] or biological enzymatic [13] methods. However, challenges associated with the dark toxicity of photosensitizers and strict requirements on pH and temperature imposed by biological cells have yet to be addressed.

Electrocatalysis have gained attention as appealing alternatives owing to their decentralized operation, simple operation and mild conditions. Electrocatalysis can readily synthesize the key precursors (e.g., H<sub>2</sub>O<sub>2</sub> and hypochlorite) necessary to achieve in situ <sup>1</sup>O<sub>2</sub> synthesis [14–17]. The efficient activation of precursors and the generation of <sup>1</sup>O<sub>2</sub> can also be achieved with the assistance of an electric field, as in the case of the electro-activation of persulfate or the electro-induced excitation of ferrocene [18]. However, substantial limitations, like system complexity, multiple byproducts and poor mass transport, must be addressed before they can be widely implemented [19].

In general, the oxygen evolution reaction (OER, Eq. 1) at the anode in conventional electrochemical systems, is commonly considered to be a

\* Corresponding author at: College of Environmental Science and Engineering, Donghua University, Shanghai 201620 China.

E-mail address: [yanbiaoliu@dhu.edu.cn](mailto:yanbiaoliu@dhu.edu.cn) (Y. Liu).

<https://doi.org/10.1016/j.apcatb.2024.123708>

Received 6 September 2023; Received in revised form 21 December 2023; Accepted 4 January 2024

Available online 6 January 2024

0926-3373/© 2024 Elsevier B.V. All rights reserved.

side reaction that does not contribute to the degradation of organic compounds and that is a major factor in decreasing the overall current efficiency [20–23]. If the evolved  $O_2$  can be effectively utilized as a sustainable source for the in situ production of  $H_2O_2$  via a  $2e^-$  oxygen reduction reaction (ORR, Eq. 2) at the cathode, the risks associated with the storage, transportation, and usage of  $H_2O_2$  can be avoided [24–26]. Furthermore, as  $H_2O_2$  is an important precursor for the electrocatalytic synthesis of  $^1O_2$ , it is feasible to achieve the targeted chain reaction of  $O_2 \rightarrow H_2O_2 \rightarrow ^1O_2$  within a single operation unit, providing a new route to improve overall system efficacy.



This new route to produce  $^1O_2$  can be realized by constructing an "O<sub>2</sub> self-feeding" fluidic sequential electrocatalytic design by coupling the OER at the anode with the ORR at the cathode. To do this, we rationally designed a sequential electrocatalytic system consisting of an IrO<sub>2</sub>-loaded Ti (IrO<sub>2</sub> @Ti) mesh anode and a carbon nanotube (CNT) filter cathode functionalized with nanoconfined Fe<sub>2</sub>O<sub>3</sub> catalyst (Fe<sub>2</sub>O<sub>3</sub>-in-CNT). The fluidic configuration of the electrocatalytic system provides convection-enhanced mass transport to boost the overall reaction kinetics [27,28]. In this design, the function of O<sub>2</sub> evolution and consumption at the anode and the cathode, respectively, as well as the concurrent generation of the key precursor H<sub>2</sub>O<sub>2</sub> for the production of  $^1O_2$ , can be achieved by precisely controlling the sequential electrochemical OER and ORR. The working mechanism and the design principles of the proposed system are determined by combining theoretical calculations and experimental results. The system efficacy is evaluated by using the antibiotic TC as a model EOC. The key process parameters are identified and optimized. The outcome of this research is dedicated to provide a viable design for the selective decontamination of EOCs from water by combining AOPs with membrane separation and electrocatalysis.

## 2. Materials and methods

### 2.1. Chemicals and reagents

Details on chemicals and materials are presented in the [Supporting Information](#) (see [Text S1](#)). All reagents were of analytical grade and used without further purification. All aqueous solution were prepared with ultrapure water produced from a Milli-Q Direct 8 purification system.

### 2.2. Preparation of electrode materials

The IrO<sub>2</sub> @Ti electrode was prepared using an electrodeposition process in a three-electrode system that contained three-electrodes [29]: a Ti mesh working electrode, an Ag/AgCl reference electrode and a Pt counter electrode ([Fig. S1](#)). The electrodeposition process was performed in the galvanostatic mode for 20 min in 100 mL of the Ir-containing precursor solution [30] ([Text S2](#)). The obtained materials were further baked at 120 °C for 10 min to yield the IrO<sub>2</sub> @Ti anode. The Fe<sub>2</sub>O<sub>3</sub>-in/out-CNT filter cathode was prepared as in our previous report with minor modification [31] ([Fig. S2](#), [Text S3](#)). Details on the characterization for electrode materials were available in [Text S4](#).

### 2.3. Electrochemical filtration experiments

Electrochemical experiments were conducted in a commercial Whatman polycarbonate filtration casing that was modified for electrochemistry ([Fig. S3](#)). The as-prepared Fe<sub>2</sub>O<sub>3</sub>-in-CNT filter and the IrO<sub>2</sub> @Ti mesh served as the cathode and anode, respectively. To eliminate any contribution of physical adsorption to on the organic removal of organic material, the electrodes were saturated with TC by passing through a 0.04 mM aqueous solution of TC through them at a flow rate of

3 mL min<sup>-1</sup> for 3 h prior to conducting any experiment. In one example of an experiment, 50 mL of an aqueous solution containing 0.04 mM TC and 10 mM Na<sub>2</sub>SiO<sub>3</sub> solution was flowed through the reactor and collected. The electric field was applied with a CHI660E electrochemical workstation (Shanghai, China) and the flow rate was controlled with an Ismatec ISM833C peristaltic pump. The electrochemical properties of the electrode materials were determined with cyclic voltammetry (CV), electrochemical impedance spectroscopy (EIS), and linear sweep voltammetry (LSV) using a three-electrode configuration.

### 2.4. Analytical methods

The TC concentration was measured using high-performance liquid chromatography (Agilent 1260 Infinity, Germany). Samples were separated on a Hypersil C18 column (4.6 × 100 mm<sup>2</sup>, 2.7 μm) using a 1.0% of formic acid/acetonitrile (65:35, v/v) mobile phase (isocratic elution) at a flow rate of 0.5 mL min<sup>-1</sup>. The detection wavelength was 280 nm. The TC degradation intermediates were identified with ultra-high performance liquid chromatography-quadrupole time-of-flight mass spectrometry on a 6500 LC/Q-TOF system (Agilent, United States). ROS generated within the system were characterized with electron paramagnetic resonance (EPR) spectroscopy using an EMXnano instrument (Bruker, Germany). An inductively coupled plasma atomic emission spectrometer (Prodigy-ICP, United States) was employed to measure the potential leakage of metal ions in the effluent.

### 2.5. Density functional theory (DFT) calculation

DFT calculations on the anode material were performed using a generalized gradient approximation function [32]. The ion–electron interaction was described with the projector augmented wave method with a kinetic energy cutoff of 520 eV [33,34]. A Monkhorst-Pack 2 × 2 × 1 *k*-point grid for the Brillouin zone was used for all supercells. A vacuum spacing of 18 Å was set along the vertical direction for the structure to avoid interactions between periodic images. The adsorption energies ( $E_{ads}$ ) were finally obtained with  $E_{ads} = E_{ad/sub} - E_{ad} - E_{sub}$ , where  $E_{ad/sub}$ ,  $E_{ad}$ , and  $E_{sub}$  are the total energies of the optimized adsorbate/substrate system, the adsorbate in the structure, and the clean substrate, respectively.

To illustrate the H<sub>2</sub>O<sub>2</sub> activation process, the Fe<sub>2</sub>O<sub>3</sub> cluster was placed inside and outside the CNT, which had a C–C bond length of 1.42 Å, thus constituting the confined and unconfined models, respectively, with a cell size of 12.30 × 25.00 × 29.90 and α, β, γ all equal to 90°. The CP2K package was used for the geometric optimization of the configuration and single-point energy calculations. The PBE exchange correlation functional of the DZVP-MOLOPT-SR-GTH basis group was used to describe the system. The self-consistent field convergence limit was set to 10<sup>-5</sup> Hartree and the DFT-D3 correction method in Grimme's scheme was adopted to represent the long-range *van der Waals* interactions.

## 3. Results and discussion

### 3.1. Electrode characterization

We aim to design a sequential electrochemical system that enables OER at the anode, which transforms O<sub>2</sub> into H<sub>2</sub>O<sub>2</sub> via  $2e^-$  ORR at the cathode, and finally produces  $^1O_2$  in the presence of the nanoconfined Fe<sub>2</sub>O<sub>3</sub>, which serves as a Fenton catalyst. To achieve this, a IrO<sub>2</sub> @Ti ([Fig. 1a](#)) anode was fabricated via an electrodeposition route, because IrO<sub>2</sub> is regarded as one of the most effective OER catalysts [29,35,36]. Scanning electron microscope (SEM) images of the anode revealed a rough surface without any visible cracks compared with that of pristine Ti mesh ([Fig. 1b](#)). EDS mapping results ([Fig. S4](#)) showed that Ir, O, and Ti were distributed uniformly across the entire architecture. To survey the chemical properties of IrO<sub>2</sub> nanoparticles, X-ray diffraction (XRD)

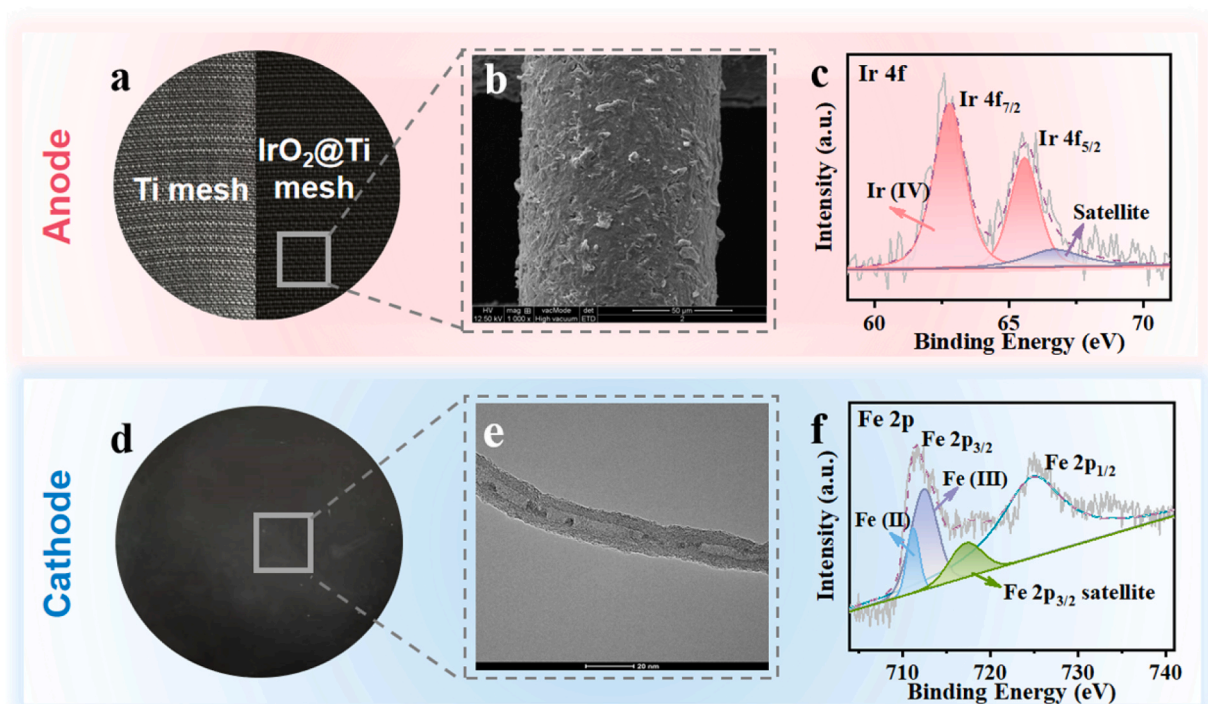


Fig. 1. (a) Photographs of pristine Ti mesh and IrO<sub>2</sub> electrodeposits on the titanium mesh. (b) SEM image of an IrO<sub>2</sub> @Ti anode. (c) Ir 4f XPS spectrum of IrO<sub>2</sub> @Ti. (d) Photograph of Fe<sub>2</sub>O<sub>3</sub>-in-CNT on a PTFE support. (e) TEM image of Fe<sub>2</sub>O<sub>3</sub>-in-CNT. (f) Fe 2p XPS pattern of Fe<sub>2</sub>O<sub>3</sub>-in-CNT.

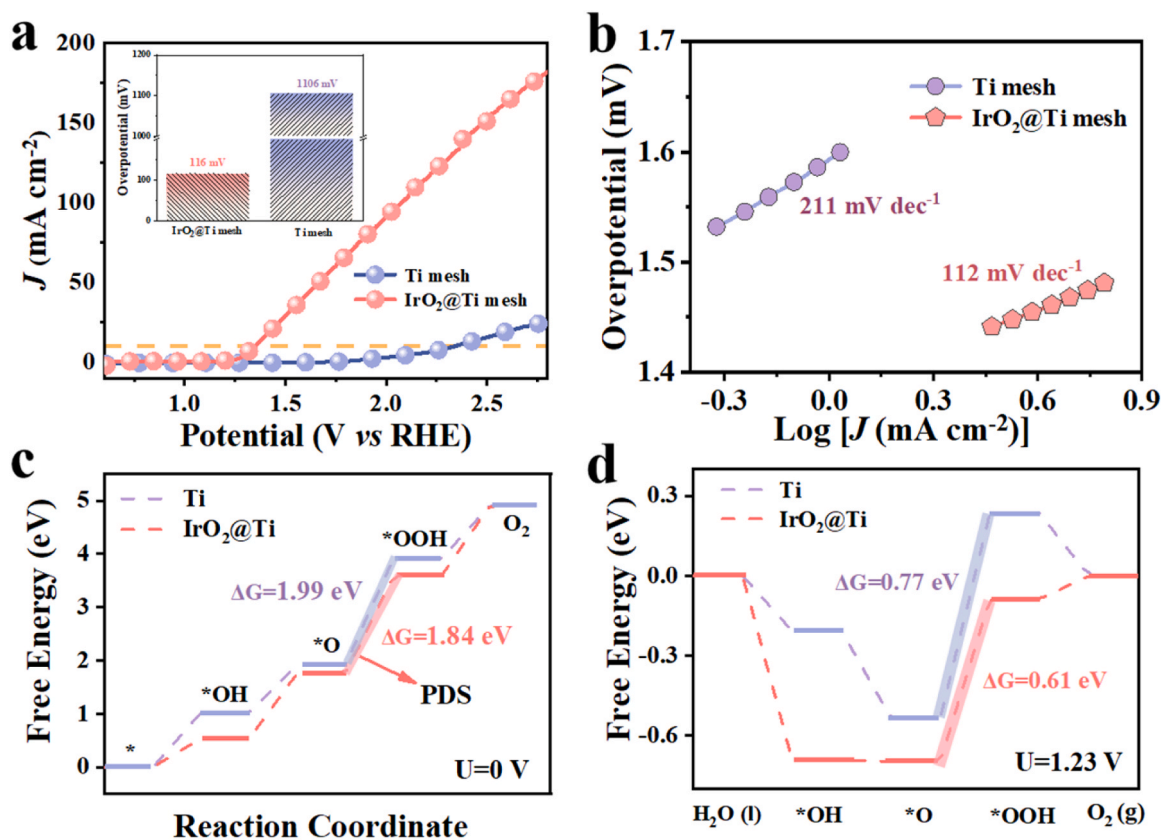


Fig. 2. (a) LSV curves of the Ti and IrO<sub>2</sub> @Ti meshes at a scan rate of 10 mV S<sup>-1</sup>. (b) Tafel plots derived from the LSV curves in 100 mM Na<sub>2</sub>SiO<sub>3</sub>. Gibbs free energy diagram for OER on Ti and IrO<sub>2</sub> @Ti surfaces at (c) U = 0 V and (d) U = 1.23 V.

and X-ray photoelectron spectroscopy (XPS) analysis were performed. As indicated in Fig. S5a, the two peaks centered at  $2\theta$  of  $34.4^\circ$  and  $40.1^\circ$  corresponded to the diffractions of the (101) and (200) planes of  $\text{IrO}_2$  (PDF 15-870), respectively. Additionally, the Ir 4f of XPS spectra showed the characteristic  $\text{Ir}^{4+}$  ( $4f_{5/2}$ ) and  $\text{Ir}^{4+}$  ( $4f_{7/2}$ ) peaks, suggesting that  $\text{Ir(IV)}$  is the dominant form of Ir on the  $\text{IrO}_2$  @Ti anode (Fig. 1c) [36].

For the cathode,  $\text{Fe}_2\text{O}_3$ -in-CNT (Fig. 1d) was prepared with the aim to utilize those anodically generated  $\text{O}_2$  to produce  $\text{H}_2\text{O}_2$  via a  $2e^-$  ORR. As shown in Fig. 1e and S6,  $\text{Fe}_2\text{O}_3$ -in-CNT had a unique nanoconfined microstructure. The  $\text{Fe}_2\text{O}_3$  nanoparticles were  $3.8 \pm 0.3$  nm in size and appeared to be uniformly dispersed within the CNT channels. The XRD patterns in Fig. S5b clearly illustrated the diffractions from the (311) and (440) crystal planes of  $\text{Fe}_2\text{O}_3$ , respectively. The Fe 2p spectrum of the fresh catalyst was deconvoluted into three subpeaks, including Fe  $2p_{1/2}$  centered at 724.8 eV and a corresponding satellite peak at 717.2 eV, indicating that the fresh  $\text{Fe}_2\text{O}_3$ -in-CNT catalyst consisted of Fe(II) and Fe (III) (Fig. 1f) [37].

### 3.2. Anodic OER

The OER activity of the different anodes was evaluated with LSV in an  $\text{O}_2$ -saturated 0.1 M  $\text{Na}_2\text{SiO}_3$  electrolyte solution at a sweep rate of  $10 \text{ mV s}^{-1}$  (Text S6-S8). Fig. 2a shows that the  $\text{IrO}_2$  @Ti anode required an overpotential of only  $\sim 116 \text{ mV}$  to achieve the current density of  $10 \text{ mA cm}^{-2}$ , outperforming of a standard Ti counterpart, which required an overpotential of  $\sim 1106 \text{ mV}$  to achieve the same current density. Inclusion of  $\text{IrO}_2$  on the Ti anode decreased by 90% the overpotential necessary to achieve a current density of  $10 \text{ mA cm}^{-2}$ , indicating that the OER activity is greatly boosted with the  $\text{IrO}_2$  @Ti anode.

In connection with the LSV, Tafel plots of the anode materials were used to compare their OER kinetics. As shown in Fig. 2b, the  $\text{IrO}_2$  @Ti anode had the smallest Tafel slope of  $112 \text{ mV dec}^{-1}$ . These results suggested the promising activity and kinetics of the  $\text{IrO}_2$  @Ti anode toward the OER.

A commonly applied approach to model the behavior of an OER typically involves  $4e^-$  processes, resulting in the production of intermediates primarily associated with  $\cdot\text{OH}$ ,  $\cdot\text{O}$ ,  $\cdot\text{OOH}$ , and  $\text{O}_2$  in acidic environment (Eqs. 3–6) [38–40]. To examine the boosting effect on the OER caused by the added  $\text{IrO}_2$ , the first-principle DFT calculations were conducted to probe the reaction energetics. To this end, heterojunction structures of Ti and  $\text{IrO}_2$  @Ti (Fig. S7) were simulated and the changes in the Gibbs free energies ( $\Delta G$ ) of each intermediate relative to the initial state at 0 and 1.23 V were calculated, as presented in Figs. 2c and 2d. Notably,  $\cdot\text{OOH}$  formation was identified as the potential-determining step for both anode materials. Based on the calculation results at 0 V, the  $\Delta G$  of  $\text{IrO}_2$  @Ti decreased to 1.83 eV at 1.23 V compared with that of Ti (1.99 eV), indicating that the in-plane heterojunction enhanced the OER activity of  $\text{IrO}_2$  @Ti. Consequently, the DFT calculation results validated that  $\text{IrO}_2$  can effectively promote the OER activity.

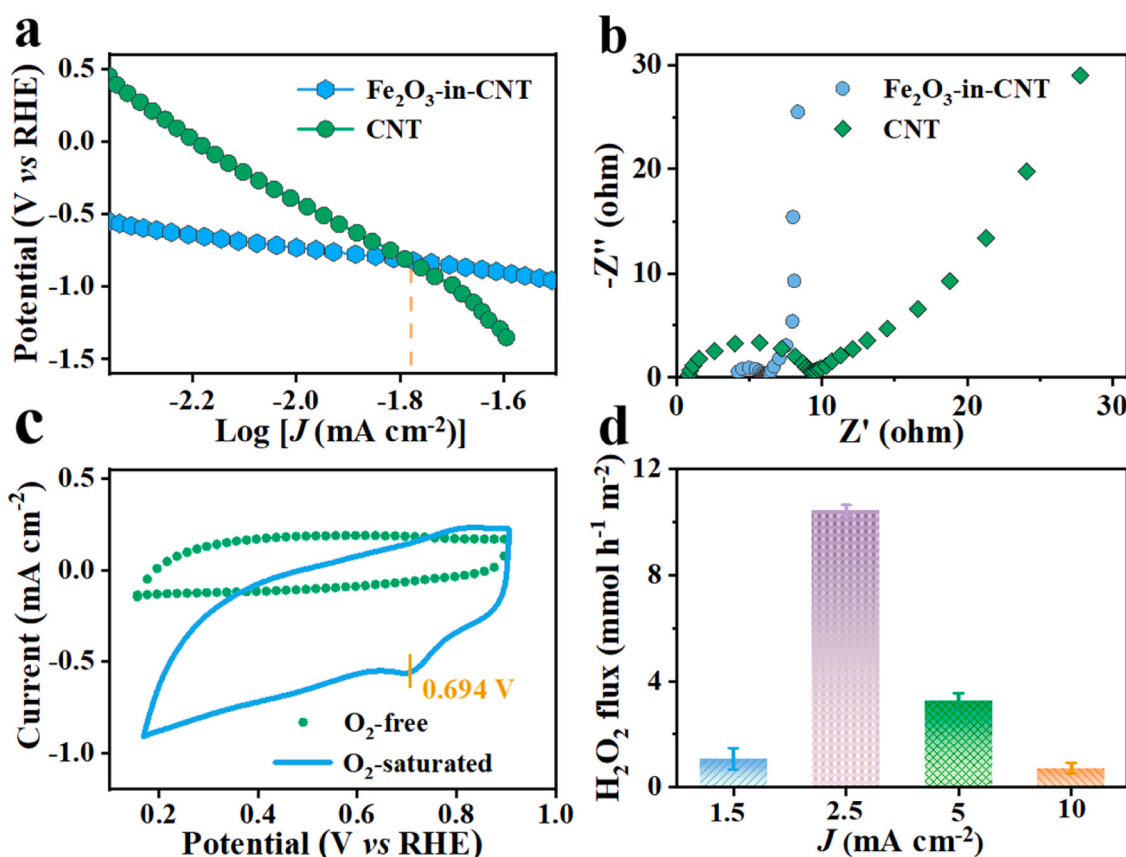


**Fig. 3.** (a) Comparison of the Tafel plots of  $\text{Fe}_2\text{O}_3$ -in-CNT and CNT in a 100 mM  $\text{Na}_2\text{SiO}_3$  solution. (b) Nyquist diagrams of the  $\text{Fe}_2\text{O}_3$ -in-CNT and CNT filters. (c) CV curves of  $\text{Fe}_2\text{O}_3$ -in-CNT filter in  $\text{O}_2$ -saturated and  $\text{O}_2$ -free 100 mM  $\text{Na}_2\text{SiO}_3$  solution at a scan rate of  $10 \text{ mV s}^{-1}$ . (d) Effect of applied current density on the  $\text{H}_2\text{O}_2$  flux of the CNT filter.



### 3.3. Cathodic ORR

In addition to the anode design, the cathode should be able to induce the  $2e^-$  ORR. Because the  $O_2/H_2O$  ratio in an aqueous solution to that of in air is only  $\sim 1:200,000$ , it is easy for standard immersed cathodes to become diffusion-limited, thereby developing a high concentration overpotential [29]. We compared our  $Fe_2O_3$ -in-CNT filter cathode with pure CNT electrode using Tafel plots (Fig. 3a), which were converted from the LSV data of Fig. S8. When a CNT electrode was tested with pure  $O_2$  bubbled directly into solution, the Tafel plot deviated from linearity at  $1.78 \text{ mA cm}^{-2}$ , which indicated the reduction of the  $O_2$  level near the electrode. However, for the  $Fe_2O_3$ -in-CNT filter cathode with purged  $O_2$ , the Tafel plot remained linear up to  $3.47 \text{ mA cm}^{-2}$ , indicating the delivery of sufficient  $O_2$  to the cathodic filter surface. Furthermore, in contrast to the pure CNT electrode (Fig. 3b), the circular arc of EIS that related to the  $Fe_2O_3$ -in-CNT filter electrode was much lower, indicating that the addition of  $Fe_2O_3$  significantly decreased the interfacial resistance and accelerated the electron transfer kinetics [41].

To monitor the evolution of anodically produced  $O_2$ , cyclic voltammetry (CV) curves of the  $Fe_2O_3$ -in-CNT cathodic filter electrode was measured to investigate the ORR behavior. As depicted in Fig. 3c, CV curves of the  $Fe_2O_3$ -in-CNT electrode in  $O_2$ -saturated (blue curve) and  $O_2$ -free (green curve) conditions were compared. For potential range of 0 to 1 V (vs RHE), the CV curves of the  $Fe_2O_3$ -in-CNT filter cathode in the  $O_2$ -free electrolyte were featureless. However, in the case of the  $O_2$ -saturated electrolyte solution, a distinct reduction peak at a potential of 0.694 V (vs RHE) on the negative-going scan could be observed, which corresponded to the reduction of  $O_2$ . The difference in the CV results demonstrated that the  $Fe_2O_3$ -in-CNT filter cathode had ORR activity, in good agreement with previous reports [31,42].

Another important property of the cathode is its  $2e^-$  ORR selectivity compared to the  $4e^-$  reduction of  $O_2$  to  $H_2O$ . Therefore, the flux of  $H_2O_2$  in the fluidic system was examined as a function of the current density using a pristine CNT filter as the cathode (Text S5, S9). The results indicated that the  $H_2O_2$  flux increased from  $1.08$  to  $10.45 \text{ mmol h}^{-1} \text{ m}^{-2}$  as the current density shifted from  $1.5$  to  $2.5 \text{ mA cm}^{-2}$ . Further increasing the current density did not provide any additional increases in the  $H_2O_2$  flux (Fig. 3d). These results suggested that the optimal current density for the  $2e^-$  ORR process was  $2.5 \text{ mA cm}^{-2}$ , and that an elevated current density could induce mass-transport limitations of  $O_2$  trapped on the  $IrO_2$  surface and thus decrease the flux of  $H_2O_2$ .

### 3.4. Concept verification

The " $O_2$  self-feeding" fluidic electrocatalytic system was constructed by employing a  $IrO_2$  @Ti mesh anode and a  $Fe_2O_3$ -in-CNT filter cathode (Fig. 4a). The  $O_2$  produced at the  $IrO_2$  @Ti mesh anode could serve as precursor for the production of  $H_2O_2$  via the  $2e^-$  ORR at the cathode, which then transformed into  $^1O_2$  in the presence of nanoconfined  $Fe_2O_3$  catalysts (Fig. 4b). TC was selected as an example EOC to assess the effectiveness of the proposed technology. As shown in Fig. 5a, a  $> 95\%$  of the TC was degraded just by circulating in the fluidic electrocatalytic system for 3 h. However, when the  $Fe_2O_3$ -in-CNT filter cathode was replaced with the  $Fe_2O_3$ -out-CNT or CNT filter cathode, the TC degradation kinetics decreased by a factor of 1.8 or 2.4, respectively, compared with that of  $Fe_2O_3$ -in-CNT filter. This quantitatively exemplified the advantages of the nanoconfined design in boosting the TC degradation kinetics. It has been reported a nanoconfined design favors the accumulation of reactants, but also changes the electronic structure in the nanoconfined environment [43,44]. Moreover, poor catalytic performance was observed when the system was purged with  $N_2$ . A slight improvement in the TC degradation efficiency occurred when the system ran on dissolved  $O_2$ . In contrast, an increase in the TC degradation kinetics was observed using the  $O_2$  produced in-situ, which was equivalent to constantly purging the system with  $O_2$  (Fig. 5b). This result indicated that a reagent-free and sustainable system running solely on electricity could be achieved for water decontamination.

Fenton-like oxidation processes are frequently employed to degrade organic pollutants for water purification. However, the quenching of radicals (e.g.,  $HO^\bullet$ ) in Fenton-like reactions by various coexisting anions and/or organic compounds limits their efficacy in industrial applications. Degradation experiment was further performed in real waters (e.g., tap water and lake water) to evaluate the potential environmental application (Fig. S9). The excellent degradation efficiency could still achieve, highlighting the practicability of the proposed process in water treatment. In addition, the selective oxidant  $^1O_2$  is less affected by the water matrices than the radicals [45]. Fig. 5c compares the removal efficiency of the  $Fe_2O_3$ -in-CNT and the  $Fe_2O_3$ -out-CNT systems in the presence of various coexisting anions, including chloride ( $Cl^-$ ), sulfate ( $SO_4^{2-}$ ) and bicarbonate ( $HCO_3^-$ ). Negligible inhibition in the  $Fe_2O_3$ -in-CNT system occurred after the spike of different competitive anions. While in the  $Fe_2O_3$ -out-CNT system that dominated by  $HO^\bullet$  [31], the addition of these coexisting anions posed a restrain effect on

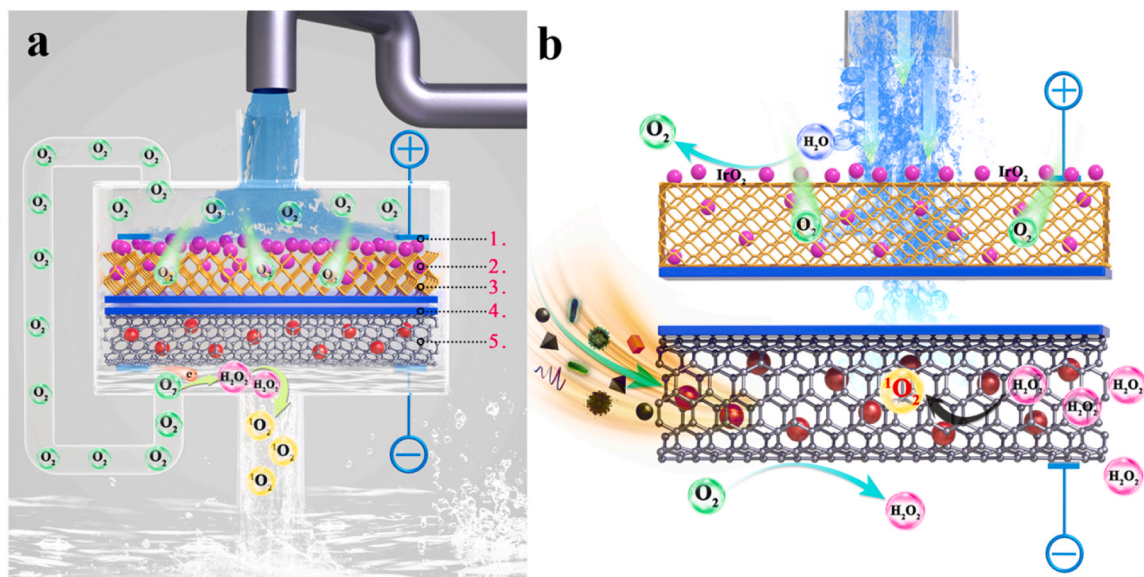


**Fig. 4.** Schematic illustrations of the system. (a) The " $O_2$  self-feeding" fluidic sequential electrocatalytic system ((1) Ti rod, (2)  $IrO_2$  nanoparticles, (3) titanium mesh, (4) PTFE substrate, (5)  $Fe_2O_3$ -in-CNT cathode). (b) The targeted chain reaction of  $O_2 \rightarrow H_2O_2 \rightarrow ^1O_2$ .

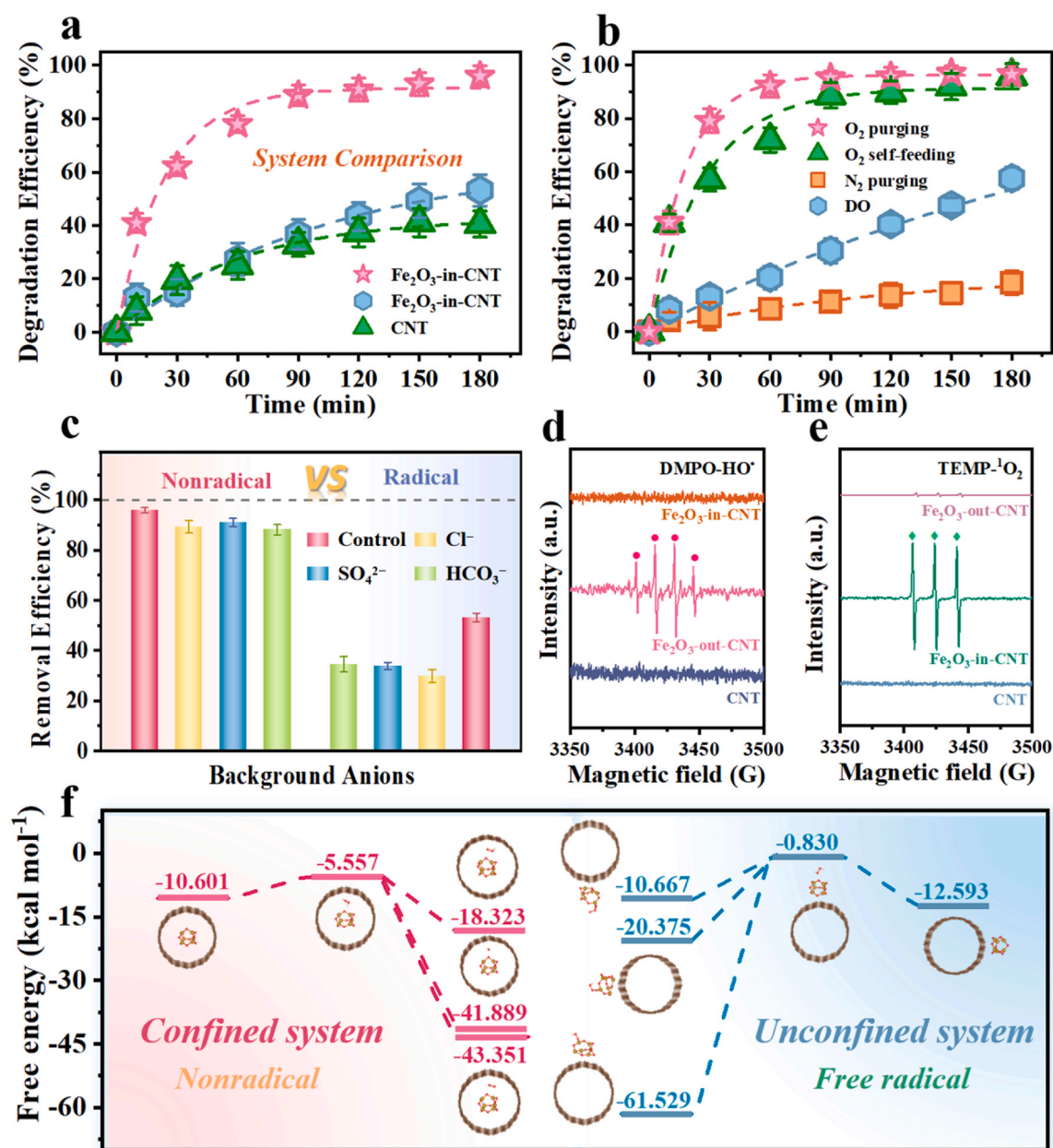


**Fig. 5.** (a) Degradation of TC in different systems. (b) The effect of O<sub>2</sub> on the degradation of TC. (c) Comparison of TC degradation in the presence of various coexisting anions. EPR characterization using (d) DMPO and (e) TEMP in the "O<sub>2</sub> self-feeding" fluidic sequential electrocatalytic system. Experimental conditions: [TC]<sub>0</sub> = 0.04 mM,  $J = 2.5 \text{ mA cm}^{-2}$ , pH = 6.5, flow rate = 3 mL min<sup>-1</sup>, and [Na<sub>2</sub>SiO<sub>3</sub>]<sub>0</sub> = 10 mM. (f) The free energy profiles of the proposed intermediates in the confined and unconfined systems.

the system efficacy by decaying the overall removal efficiency of TC by 18–25%. Hence, the excellent anti-interference ability of the nano-confined electrode enables a continuous, integrated and selective water decontamination. To optimize the operational conditions, the effects of several important operational parameters, such as pH, electrolytes, Fe<sub>2</sub>O<sub>3</sub> loading level, and current density, on the performance of the system were investigated and optimized (Fig. S10). These results indicated that a neutral pH condition and a mild current density would boost the oxidation kinetics, while an excess loading of Fe<sub>2</sub>O<sub>3</sub> would deteriorate the overall TC degradation efficiency. Considering the practical application feasibility, the long-term system stability of the proposed technology was evaluated by continuous running for 30 h. Results suggested that the TC removal efficiency was still > 85% after the test (Fig. S11). A simple chemical washing with diluted NaOH solution enables effective regeneration of the cathodic filter, as evidenced by the

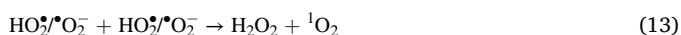
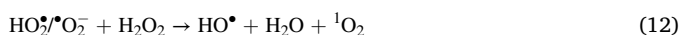
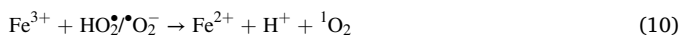
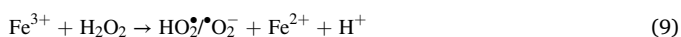
90.3% TC removal after eight successive running cycles as well as the limited iron leaching ( $\leq 0.01 \text{ mg L}^{-1}$ ). Such promising results was comparable or even better than several state-of-the-art electrochemical systems (Table S1).

### 3.5. Mechanistic insights

To determine the active species involved in the degradation of TC, radical quenching experiments were performed by spiking TBA and FFA. TBA and FFA functioned as a radical scavenger for HO• and as a quencher for <sup>1</sup>O<sub>2</sub>, respectively. As shown in Fig. S12, the TC removal efficiency decreased to 15.7% when TBA was included in the Fe<sub>2</sub>O<sub>3</sub>-out-CNT system, while the addition of FFA had a negligible impact on the TC degradation. These results revealed that HO• played a significant role in the Fe<sub>2</sub>O<sub>3</sub>-out-CNT system, as observed in our previous report [31].

However, the addition of FFA in the Fe<sub>2</sub>O<sub>3</sub>-in-CNT system significantly inhibited the degradation of TC, implying that the most important species for the removal of TC was non-radical <sup>1</sup>O<sub>2</sub>. In addition, EPR technique was conducted complementarily to examine the active species using DMPO and TEMP as the probes of HO• and <sup>1</sup>O<sub>2</sub>, respectively. As shown in Figs. 5d and 5e, there was no definable signal when pristine CNT was used as the filter cathode, indicating that the ROS were at most produced only minimally without the Fe<sub>2</sub>O<sub>3</sub>. The EPR spectrum showed the signal of the DMPO-HO• adduct (height ratio = 1:2:2:1) in the Fe<sub>2</sub>O<sub>3</sub>-out-CNT system. In stark contrast, the TEMP-<sup>1</sup>O<sub>2</sub> adduct (height ratio = 1:1:1) in the Fe<sub>2</sub>O<sub>3</sub>-in-CNT system indicated the formation of <sup>1</sup>O<sub>2</sub>.

High-resolution XPS of Fe was used to determine the mechanism involved in the acceleration of the Fe(II)/Fe(III) redox cycle during the electrocatalytic process (Fig. S13). Noticeably, in contrast to the fresh Fe<sub>2</sub>O<sub>3</sub>-in-CNT catalyst, the Fe(II)/Fe(III) ratio decreased from 30.5% to 22.3% in the absence of electric field. When an electric field was applied, the content of Fe(III) of the used catalyst decreased significantly from 76.8% to 36.3%, while the Fe(II) content increased from 23.3% to 30.7% after 3 h of the catalytic reaction. These results verified the critical role of the electric field in terms of mediating the cycling of Fe(II/III) pairs, which promoted the production of active species (Eqs. 7–14).



To gain insights into the working mechanism of the system, we employed a DFT-based theoretical calculation to model the reaction with different cathode materials. The adsorption energy of H<sub>2</sub>O<sub>2</sub> adsorbed in the Fe<sub>2</sub>O<sub>3</sub>-in-CNT and Fe<sub>2</sub>O<sub>3</sub>-out-CNT systems were calculated to be −5.557 and −0.830 kcal mol<sup>−1</sup>, respectively, indicating H<sub>2</sub>O<sub>2</sub> is more readily adsorbed in the nanoconfined system. In addition, the free energy also was calculated to assess the stability of each system. As shown in Fig. 5f, in the Fe<sub>2</sub>O<sub>3</sub>-in-CNT system, the energy barrier for the formation of <sup>1</sup>O<sub>2</sub> is lower than that of HO• (−41.889 kcal mol<sup>−1</sup>) and HO<sub>2</sub>• (−18.323 kcal mol<sup>−1</sup>). In the Fe<sub>2</sub>O<sub>3</sub>-out-CNT system, the energy profile showed that the decomposition of H<sub>2</sub>O<sub>2</sub> adsorbed in the Fe<sub>2</sub>O<sub>3</sub>-out-CNT could generate HO• with an energy barrier of −61.529 kcal mol<sup>−1</sup>. These findings agreed with the results of the experiments, implying that the formation of <sup>1</sup>O<sub>2</sub> is thermodynamically favorable in the spatial nanoconfinement. A plausible underlying working mechanism and possible TC degradation pathways for the system are presented in Figs. 4b, S14 and S15.

#### 4. Conclusion

We proposed the principle and method of constructing a "O<sub>2</sub> self-feeding" fluidic sequential electrocatalytic system to selective decontaminate aqueous EOC in this study. We revealed the working mechanism of the proposed system and the synergic effects between the electrodes and clarified the relevant mechanisms of nanoconfined Fenton catalysts for the targeted formation of <sup>1</sup>O<sub>2</sub>. This will enable efficient removal of EOCs from water and therefore has significant scientific and academic values. We developed new insights for the selective decontamination of EOCs in complex water quality conditions, thus, demonstrating the important engineering value and environmental significance

of this work.

In addition, since several available electrochemical redox couples involving with electron coupling process, our proposed fluidic sequential electrochemical system provides a versatile platform that could be implemented in various practical scenarios in environmental applications (such as resource recovery and pollutants remediation). It is of note that the overall system efficiency and energy requirements could be further mitigated by incorporating other electrochemical redox couples with rapid reaction kinetics and limited overpotentials. Both reactor design, electrode materials, and operational parameters could be further optimized to boost the EOC decontamination efficiency for practical deployments.

#### CRediT authorship contribution statement

**You Shijie:** Writing – review & editing. **Liu Yanbiao:** Conceptualization, Supervision, Writing – review & editing. **Zheng Wentian:** Methodology, Validation. **Sun Meng:** Validation. **Xie Mengjiao:** Data curation, Investigation, Methodology, Writing – original draft.

#### Declaration of Competing Interest

The authors declare that they have no known competing financial interests or personal relationships that could have appeared to influence the work reported in this paper.

#### Data availability

Data will be made available on request.

#### Acknowledgements

Project was supported by the National Natural Science Foundation of China (No. 52170068), the Natural Science Foundation of Shanghai (23ZR1401300) and the Fundamental Research Funds for the Central Universities (2232023A-08). The authors also acknowledge the Analytical and Testing Centre of Donghua University for materials characterization.

#### Appendix A. Supporting information

Supplementary data associated with this article can be found in the online version at doi:10.1016/j.apcatb.2024.123708.

#### References

- [1] M.M. Zhong, T.L. Wang, W.X. Zhao, J. Huang, B. Wang, L. Blaney, Q.W. Bu, G. Yu, Emerging organic contaminants in chinese surface water: Identification of priority pollutants, *Engineering* 11 (2022) 111–125.
- [2] J. Garcia, G.M.J. Garcia, J.W. Day, R. Boopathy, J.R. White, S. Wallace, R. G. Hunter, A review of emerging organic contaminants (EOCs), antibiotic resistant bacteria (ARB), and antibiotic resistance genes (ARGs) in the environment: increasing removal with wetlands and reducing environmental impacts, *Bioresour. Technol.* 307 (2020) 123228.
- [3] Y.B. Liu, F. Li, Q. Xia, J.W. Wu, J.S. Liu, M.Z. Huang, J.P. Xie, Conductive 3D sponges for affordable and highly-efficient water purification, *Nanoscale* 10 (2018) 4771–4778.
- [4] D.J. Lapworth, N. Baran, M.E. Stuart, R.S. Ward, Emerging organic contaminants in groundwater: a review of sources, fate and occurrence, *Environ. Pollut.* 163 (2012) 287–303.
- [5] Y. Zhou, J. He, X. Li, J. Lu, Y.B. Zhou, Efficient removal of roxarsone and emerging organic contaminants by a solar light-driven in-situ Fenton system, *Chem. Eng. J.* 435 (2022) 132434.
- [6] L.Y. Xing, J. Wei, Y.F. Zhang, M.D. Xu, G.P. Pan, J.M. Li, J. Li, Y.N. Li, Boosting active sites of progenetic sludge-based biochar by boron doping for electro-Fenton degradation towards emerging organic contaminants, *Sep. Purif. Technol.* 294 (2022) 121160.
- [7] H. Kim, W. Kim, Y. Mackeyev, G.S. Lee, H.J. Kim, T. Tachikawa, S. Hong, S. Lee, J. Kim, L.J. Wilson, T. Majima, P.J. Alvarez, W. Choi, J. Lee, Selective oxidative degradation of organic pollutants by singlet oxygen-mediated photosensitization: tin porphyrin versus C<sub>60</sub> aminofullerene systems, *Environ. Sci. Technol.* 46 (2012) 9606–9613.



- [8] S.S. Zhu, X.J. Li, J. Kang, X.G. Duan, S.B. Wang, Persulfate activation on crystallographic manganese oxides: mechanism of singlet oxygen evolution for nonradical selective degradation of aqueous contaminants, *Environ. Sci. Technol.* (2022).
- [9] Z. Li, Y. Sun, Y. Yang, Y. Han, T. Wang, J. Chen, D.C.W. Tsang, Comparing biochar- and bentonite-supported Fe-based catalysts for selective degradation of antibiotics: mechanisms and pathway, *Environ. Res.* 183 (2020) 109156.
- [10] Q.Y. Yi, J.H. Ji, B. Shen, C.C. Dong, J.J. Liu, J.L. Zhang, M.Y. Xing, Singlet oxygen triggered by superoxide radicals in a molybdenum cocatalytic Fenton reaction with enhanced REDOX activity in the environment, *Environ. Sci. Technol.* 53 (2019) 9725–9733.
- [11] M.X. Cheng, Y.C. Zhang, B. Lai, L.Z. Wang, S.J. Yang, K.L. Li, D.Q. Wang, Y.G. Wu, G.H. Chen, J. Qian, Nitrogen and phosphorus co-doped porous carbons (NPCs) for peroxydisulfate (PDS) activation towards tetracycline degradation: defects enhanced adsorption and non-radical mechanism dominated by electron transfer, *Chem. Eng. J.* 455 (2023) 140615.
- [12] S. Tanaka, T. Enoki, H. Imoto, Y. Ooyama, J. Ohshita, T. Kato, K. Naka, Highly efficient singlet oxygen generation and high oxidation resistance enhanced by arsole-polymer-based photosensitizer: application as a recyclable photooxidation catalyst, *Macromolecules* 53 (2020) 2006–2013.
- [13] K.N. Ingenbosch, S. Quint, M. Dyllick-Brenzinger, D.S. Wunschik, J. Kiebitz, P. Suss, U. Liebelt, R. Zuhse, U. Menyes, K. Scheibner, C. Mayer, K. Opwis, J. S. Gutmann, K. Hoffmann-Jacobsen, Singlet-oxygen generation by peroxidases and peroxygenases for chemoenzymatic synthesis, *ChemBioChem* 22 (2021) 398–407.
- [14] Z. Liu, H. Ding, C. Zhao, T. Wang, P. Wang, D.D. Dionysiou, Electrochemical activation of peroxymonosulfate with ACF cathode: kinetics, influencing factors, mechanism, and application potential, *Water Res.* 159 (2019) 111–121.
- [15] D.L. Guo, Y.B. Liu, Singlet oxygen-mediated electrochemical reaction for selective and rapid degradation of organic compounds, *Ind. Eng. Chem. Res.* 59 (2020) 14180–14187.
- [16] Q.Z. Zhang, M.H. Zhou, G. Ren, Y.W. Li, Y.C. Li, X.D. Du, Highly efficient electrosynthesis of hydrogen peroxide on a superhydrophobic three-phase interface by natural air diffusion, *Nat. Commun.* 11 (2020) 1731.
- [17] C.A. Martinez, E. Brillas, Electrochemical alternatives for drinking water disinfection, *Angew. Chem. Int. Ed.* 47 (2008) 1998–2005.
- [18] C.Y. Nie, Z.M. Ao, X.G. Duan, C.Y. Wang, S.B. Wang, T.C. An, Degradation of aniline by electrochemical activation of peroxydisulfate at MWCNT cathode: the proofed concept of nonradical oxidation process, *Chemosphere* 206 (2018) 432–438.
- [19] S.C. Tian, Y.B. Li, H.B. Zeng, W. Guan, Y. Wang, X. Zhao, Cyanide oxidation by singlet oxygen generated via reaction between  $\text{H}_2\text{O}_2$  from cathodic reduction and  $\text{OCl}^-$  from anodic oxidation, *J. Colloid Interface Sci.* 482 (2016) 205–211.
- [20] N.K. Shrestha, S.A. Patil, J.H. Han, S. Cho, A.I. Inamdar, H. Kim, H. Im, Chemical etching induced microporous nickel backbones decorated with metallic Fe@hydroxide nanocatalysts: an efficient and sustainable OER anode toward industrial alkaline water-splitting, *J. Mater. Chem. A* 10 (2022) 8989–9000.
- [21] L. Li, X.J. Cao, J.J. Huo, J.P. Qu, W.H. Chen, C.T. Liu, Y.F. Zhao, H. Liu, G.X. Wang, High valence metals engineering strategies of Fe/Co/Ni-based catalysts for boosted OER electrocatalysis, *J. Energy Chem.* 76 (2023) 195–213.
- [22] Z.H. Pei, H.B. Zhang, Z.P. Wu, X.F. Lu, D.Y. Luan, X.W. Lou, Atomically dispersed Ni activates adjacent Ce sites for enhanced electrocatalytic oxygen evolution activity, *Sci. Adv.* 9 (2023) 1320.
- [23] H. Shen, T.R. Wei, Q. Liu, S.S. Zhang, J. Luo, X.J. Liu, Heterogeneous Ni-MoN nanosheet-assembled microspheres for urea-assisted hydrogen production, *J. Colloid Interface Sci.* 634 (2023) 730–736.
- [24] Y.S. Zhu, F.X. Deng, S. Qiu, F. Ma, Y.S. Zheng, L. Gao, A self-sufficient electro-Fenton system with enhanced oxygen transfer for decontamination of pharmaceutical wastewater, *Chem. Eng. J.* 429 (2022) 132176.
- [25] G.C. da Silva, M.R. Fernandes, E.A. Ticianelli, Activity and stability of Pt/IrO<sub>2</sub> bifunctional materials as catalysts for the oxygen evolution/reduction reactions, *ACS Catal.* 8 (2018) 2081–2092.
- [26] C. Xia, J.Y. Kim, H.T. Wang, Recommended practice to report selectivity in electrochemical synthesis of  $\text{H}_2\text{O}_2$ , *Nat. Catal.* 3 (2020) 605–607.
- [27] S. Moon, P. Vineeth, W.L. Yang, S.V. Johannes, C.A. Gorski, B.E. Logan, Improving the thermodynamic energy efficiency of battery electrode deionization using flow-through electrodes, *Environ. Sci. Technol.* 54 (2020) 3628–3635.
- [28] Y.J. Zhou, G. Zhang, Q.H. Ji, W. Zhang, J.Y. Zhang, H.J. Liu, J.H. Qu, Enhanced stabilization and effective utilization of atomic hydrogen on Pd-In nanoparticles in a flow-through electrode, *Environ. Sci. Technol.* 53 (2019) 11383–11390.
- [29] J.W. Xu, X.L. Zheng, Z.P. Feng, Z.Y. Lu, Z.W. Zhang, W. Huang, Y.B. Li, D. Vuckovic, Y.Q. Li, S. Dai, G.X. Chen, K.C. Wang, H.S. Wang, J.K. Chen, W. Mitch, Y. Cui, Organic wastewater treatment by a single-atom catalyst and electrolytically produced  $\text{H}_2\text{O}_2$ , *Nat. Sustain.* 4 (2021) 233–241.
- [30] K. Y, Anodically electrodeposited iridium oxide films (AEIROF) from alkaline solution for electrochromic display devices, *Jpn. J. Appl. Phys.* 28 (1989).
- [31] D.L. Guo, Y.B. Liu, H.D. Ji, C.C. Wang, B. Chen, C.S. Shen, F. Li, Y.X. Wang, P. Lu, W. Liu, Silicate-enhanced heterogeneous flow-through electro-Fenton system using iron oxides under nanoconfinement, *Environ. Sci. Technol.* 55 (2021) 4045–4053.
- [32] J.P. Perdew, K. Burke, M. Ernzerhof, Generalized gradient approximation made simple, *Phys. Rev. Lett.* 77 (1996) 18.
- [33] P.E. Blochl, Projector augmented-wave method, *Phys. Rev. B Condens. Matter* 50 (1994) 17953–17979.
- [34] G. Kresse, D. Joubert, From ultrasoft pseudopotentials to the projector augmented-wave method, *Phys. Rev. B Condens. Matter* 59 (1999) 3.
- [35] S. Czoska, K. Ehelebe, J. Geppert, L.D. Escalera, A. Bounnov, E. Saraçi, B. Mayerhöfer, U. Krewer, S. Cherevko, J.D. Grunwaldt, Heating up the OER: investigation of IrO<sub>2</sub> OER catalysts as function of potential and temperature, *ChemElectroChem* 9 (2022).
- [36] T. Audichon, T.W. Napporn, C. Canaff, C. Morais, C. Comminges, K.B. Kokoh, IrO<sub>2</sub> coated on RuO<sub>2</sub> as efficient and stable electroactive nanocatalysts for electrochemical water splitting, *J. Phys. Chem. C* 120 (2016) 2562–2573.
- [37] L.M. Jin, S.J. You, X.G. Duan, Y. Yao, J.M. Yang, Y.B. Liu, Peroxymonosulfate activation by Fe<sub>3</sub>O<sub>4</sub>-MnO<sub>2</sub>/CNT nanohybrid electroactive filter towards ultrafast micropollutants decontamination: performance and mechanism, *J. Hazard. Mater.* 423 (2022) 127111.
- [38] H. Jung, S. Choung, J.W. Han, Design principles of noble metal-free electrocatalysts for hydrogen production in alkaline media: combining theory and experiment, *Nanoscale Adv.* 3 (2021) 6797–6826.
- [39] J.D. Blakemore, R.H. Crabtree, G.W. Brudvig, Molecular catalysts for water oxidation, *Chem. Rev.* 115 (2015) 12974–13005.
- [40] D.W. Shaffer, Y. Xie, J.J. Concepcion, O-O bond formation in ruthenium-catalyzed water oxidation: single-site nucleophilic attack vs O-O radical coupling, *Chem. Soc. Rev.* 46 (2017) 6170–6193.
- [41] F.Q. Liu, Y.B. Liu, C.S. Shen, F. Li, B. Yang, M.H. Huang, C.Y. Ma, M. Yang, Z. W. Wang, W. Sand, One-step phosphite removal by an electroactive CNT filter functionalized with TiO<sub>2</sub>/CeO<sub>x</sub> nanocomposites, *Sci. Total Environ.* 710 (2020) 135514.
- [42] D.L. Guo, S.T. Jiang, L.M. Jin, K. Huang, P. Lu, Y.B. Liu, CNT encapsulated MnOx for an enhanced flow-through electro-Fenton process: the involvement of Mn(IV), *J. Mater. Chem. A* 10 (2022) 15981–15989.
- [43] Q.V. Ly, L.L. Cui, M.B. Asif, W. Khan, L.D. Nghiem, Y. Hwang, Z.H. Zhang, Membrane-based nanoconfined heterogeneous catalysis for water purification: a critical review, *Water Res.* 230 (2023) 119577.
- [44] J.S. Qian, X. Gao, B.C. Pan, Nanoconfinement-mediated water treatment: from fundamental to application, *Environ. Sci. Technol.* 54 (2020) 8509–8526.
- [45] T. Liu, S. Xiao, N. Li, J. Chen, X. Zhou, Y. Qian, C.H. Huang, Y. Zhang, Water decontamination via nonradical process by nanoconfined Fenton-like catalysts, *Nat. Commun.* 14 (2023) 2881.